PHYSICAL REVIEW B **104**, 045149 (2021)

Colossal electroresistance response accompanied by metal-insulator transition in a mixed-valent vanadate

Rafikul Ali Saha,[1,*] Abhisek Bandyopadhyay,[1,2,*] Irene Schiesaro,[3] Arnab Bera,[4] Mintu Mondal,[4]
Carlo Meneghini,[3] and Sugata Ray[1,†]
[1]*School of Materials Sciences, Indian Association for the Cultivation of Science,*
2A & 2B Raja S. C. Mullick Road, Jadavpur, Kolkata 700032, India
[2]*Department of Physics, Indian Institute of Science Education and Research, Dr. Homi Bhabha Road, Pune 411008, India*
[3]*Dipartimento di Scienze, Universitá Roma Tre, Via della Vasca Navale, 84 I-00146 Roma, Italy*
[4]*School of Physical Sciences, Indian Association for the Cultivation of Science, Kolkata 700032, India*

(Received 5 February 2021; revised 12 June 2021; accepted 14 July 2021; published 29 July 2021)

Colossal electroresistance (CER) in manganites, i.e., a large change in electrical resistance as a function of varying applied electric field or applied electric current, has often been described as complimentary to the colossal magnetoresistance (CMR) effect. Mixed valence vanadates with active t_{2g} and empty e_g orbitals, unlike manganites, have not naturally been discussed in this context, as double exchange based CMR is not realizable in them. However, presence of coupled spin and orbital degrees of freedom, metal-insulator transition (MIT) accompanied by orbital order-disorder transition, still make the vanadates important. Here we probe a Fe-doped hollandite lead vanadate $\mathrm{PbFe_{1.75}V_{4.25}O_{11}}$ (PFVO), which exhibits a clear MIT as a function of temperature. Most importantly, a giant fall in the resistivity, indicative of a CER, as well as a systematic shift in the MIT towards higher temperatures are observed with increasing applied current. Detailed structural, magnetic, thermodynamic, and transport studies point towards a complex interplay between the structural distortion, orbital order/disorder effect, and the resultant MIT and magnetic ordering in this system.

DOI: 10.1103/PhysRevB.104.045149

I. INTRODUCTION

The orbital degrees of freedom (ODF) of the correlated $3d$ transition metal oxides (TMOs), with metal-oxygen octahedral building blocks, has been one of the most fascinating condensed matter research topics for decades now. It offers a plethora of novel and extraordinary physical properties, e.g., metal-insulator transition (MIT), colossal magneto- and electroresistance, magnetization reversal, electronic phase separation, ferroelectricity, spin-glass freezing, spin, charge, orbital ordering, etc. [1–4], where the ODF determines the electron density distribution and hence, provides a link between magnetism and the chemical bonds [5]. The ODF in a solid can be manipulated via (i) the orbital-lattice Jahn-Teller (JT) coupling, (ii) the magnetic exchange interactions between the orbitals, (iii) the spin-orbit coupling, and (iv) extrinsic effects due to ionic size mismatch of cations, external applied pressure, presence of lone pair, etc. [5–7]. In case of strong JT interaction (active orbitals of e_g symmetry) the completely uncorrelated spin and orbital degrees of freedom could facilitate very different magnetic and structural transition temperatures within larger lattice distortions [7]. On the other hand, the t_{2g}-active orbitals (Ti, V, Ru, etc.) possess weak JT distortions, and consequently, strong competition between the spin interactions and the orbital ordering/disordering phenomena may produce nearly coinciding magnetic and structural transition temperatures [7]. It is worth mentioning to state that the manganites with e_g active orbitals show an orbital order-disorder phase transition at high temperatures at about 800 K, below which a large, of the order of 15%, distortion of octahedra sets in, indicating the dominant role of a cooperative JT physics, which is natural for e_g orbital systems with strong coupling between the oxygen vibrations and e_g quadrupole. In contrast, no cooperative structural phase transition has so far been observed in early $3d$ TMOs (Ti, V), suggesting the prevalent small lattice distortions in these compounds to be mostly due to the ionic-size mismatch effects, as t_{2g}-orbital JT coupling is weak [7]. Therefore, the lattice driven classical orbital picture, as in manganites, is contrasted by the quantum behavior of orbitals in frustrated exchange interaction models of the early $3d$ TMOs.

Naturally, vanadates are considered to be model canonical systems for investigating a rich variety of outstanding magnetic and electrical properties originating from the interconnected knot of spin, charge, orbital and lattice correlations of the V t_{2g} electrons [8–15]. The t_{2g} valence electrons of the V ions ($\mathrm{V^{3+}}$: t_{2g}^2/$\mathrm{V^{4+}}$: t_{2g}^1) undergo significantly lower noncubic crystal field splitting, as compared to that of the e_g manifold in isostructural manganites, resulting in the comparable energy separation of orbital levels to the spin interactions [7,11]. Hence, the interplay between orbital and spins, (not only the intersite exchange interaction but also the intra-atomic spin-orbit interaction) becomes more pronounced within orbitally active V t_{2g} electrons [16–19] of the vanadates, causing multiple magnetic and orbital ordering transitions, accompanying with the orbital ordering/disordering-induced MIT [11–13].

---

[*] These authors equally contributed to this work.

[†] mssr@iacs.res.in

In such a backdrop, another extremely fascinating series of mixed-valence R-block-type vanadates of general chemical formula AV_6O_{11} (A = K, Na, Sr, Pb) [20–23] appear truly promising for exploring a variety of intriguing magnetic and electronic properties. The monovalent A-site ion (K^+, Na^+), as well as the divalent ones (Sr^{2+}, Pb^{2+}), all exhibit a common structural phase transition from high-temperature centrosymmetric ($P6_3/mmc$) to low-temperature noncentrosymmetric ($P6_3mc$) structure, triggered by cationic size mismatch and lone pair effect, respectively [20–23]. The magnetic ordering temperatures (T_C = 64.2, 66.8, 73, and 90 K for the A = Na, K, Sr, and Pb, respectively) are quite apart from the structural transition temperatures but are intimately accompanied with the slope change in the respective electrical resistivity vs temperature curves [23–26], which might be indicative of significant spin-lattice-orbital coupling of the orbitally active V t_{2g} electrons [7] at the onset of magnetic transition. Surprisingly, the temperature-dependent electrical resistivity measurements revealed a semiconducting/insulating behavior for the $A^{2+}V_6O_{11}$ ($A = Sr^{2+}$ and Pb^{2+}) in contrast with the metallic transport of the monovalent Na, K members [23,26]. Clearly the direct difference between the divalent and monovalent A cation members are, (1) difference in effective V^{3+}/V^{4+} ratio and the consequent carrier density (V^{3+}:V^{4+} = 2:1 for A^{2+} and 1:1 for A^+) [23,26], and (2) the difference in the A cation size and the resultant structural distortion. One option to independently probe these parameters could be to dope the V atoms in a way so that the V^{3+}/V^{4+} ratio are manipulated, keeping the A cation unchanged. Therefore, it becomes an exciting proposition to replace some proportion of V^{3+} of a $A^{2+}V_6O_{11}$ compound by the isovalent Fe^{3+} species, and taking the average V oxidation state close to ∼3.5, i.e., similar to A^+ members, thereby making the doped compounds a fertile ground for investigating new physics. However, such a strategy has its own weaknesses because the dopant ion will have different electronic structure (e.g., active e_g orbital for Fe^{3+}, unlike V^{3+}) and consequent differences in spin, orbital, and lattice degrees of freedom. Moreover, such changes around the dopant would also alter the magnetic exchange pathways and as a result, the global magnetic order may get interrupted by the local intervention of the dopant ions.

$PbFe_{1.75}V_{4.25}O_{11}$ (PFVO) becomes important in this context, where PFVO can be treated as an effectively hole-doped counterpart of the parent PbV_6O_{11}, with the resultant V^{3+}:V^{4+} ratio being nearly 1:1. Even though the parent PbV_6O_{11} is an insulator, the first exciting observation that we record in PFVO is an entry to a metallic state at around the magnetic transition temperature from the high-temperature insulating phase. This indicates that metallic transport in the system is predominantly determined by the effective V^{3+}:V^{4+} ratio, because Fe-doping ensures only this change. On the other hand, the magnetic responses of PFVO and that of parent PbV_6O_{11} (Fig. 5 of Ref. [26]) appear very similar, excepting the observation of clear hysteresis between the field-cooled cooling (FCC) and field-cooled heating (FCH) data in PFVO. However, a surprising observation is the existence of colossal electroresistance in this compound, exactly around the onset of MIT, as a function of applied electric current, which has never been anticipated for a t_{2g}-active lower transition metal system. Absence of any magnetoresistance in the system, even around the MIT, clearly establishes that the observed CER is not connected with any magnetic field driven transition of the ground state. The relative competition between the Jahn-Teller (JT) distortion along with orbital order-disorder phenomena based on the basal plane off centering of the vanadium ions, controlling movements of the doped holes, turns out to be at the root of all the emerged unusual behaviors.

II. EXPERIMENTAL TECHNIQUES

Polycrystalline $PbFe_{1.75}V_{4.25}O_{11}$ has been prepared by following the conventional solid-state reaction technique. Stoichiometric amounts of high purity (Sigma-Aldrich 99.99%) PbO and V_2O_5 have been thoroughly mixed, ground, and the mixture was then initially calcined at 600 °C in air for 48 hours, resulting in the formation of phase pure $Pb_2V_2O_7$ as the intermediate compound. Next, the as prepared $Pb_2V_2O_7$ was added stoichiometrically with high purity Fe_2O_3 and V_2O_3 in exact proportions. All these starting materials were then mixed and ground homogeneously in an agate mortar, and subsequently, this mixture was taken to form a cold-pressed hard pellet. This pellet was then fully wrapped using a platinum foil. Finally, the covered pellet was calcined at 850 °C for 12 hours in a vacuum-sealed ($\sim10^{-3}$ milibar) quartz tube, followed by quench cooling to the room temperature.

Structural characterization of the prepared sample was performed at room temperature using synchrotron x-ray radiation facility at MCX Beam-line of the Elettra synchrotron radiation facility, Italy, with wavelength $\lambda = 0.827$ Å, and low-temperature (15 K) synchrotron x-ray diffraction (XRD) has been carried out using synchrotron x-ray radiation facility at KEK photon factory, Japan, with wavelength $\lambda = 0.786$ Å. The obtained x-ray diffraction data were analyzed via Rietveld refinement using FULLPROF program [27]. To verify homogeneity and any off-stoichiometry in the sample, energy dispersive x-ray (EDX) analysis was also performed using a field emission scanning electron microscope (JEOL, JSM-7500F). The Fe- and V K-edge x-ray absorption spectra of the studied sample have been measured at the XAFS beam line of ELETTRA (Trieste, Italy) synchrotron radiation facility at room temperature in standard transmission geometry using a double crystal Si(311) monochromator [28]. Data treatment and quantitative analysis of both the Fe and V K-edge extended x-ray absorption fine structure (EXAFS) spectra were carried out using the Estra and Fitexa software [29] applying a multishell data refinement procedure [30,31] implemented considering an average Fe and V local atomic structure model calculated on the basis of the XRD Rietveld refinement results. Further, both the dc and ac magnetic susceptibility measurements in the temperature range 2–300 K were performed using a superconducting quantum interference device (SQUID) magnetometer (Quantum Design, USA) and vibrating sample magnetometer (Quantum Design, USA). In case of dc magnetization, magnetic fields were applied up to ±5 Tesla. The temperature-dependent electrical resistivity was measured by standard four-probe method within a temperature range 15–300 K in a physical property measurement system (PPMS, Quantum Design, USA) and in a laboratory-based

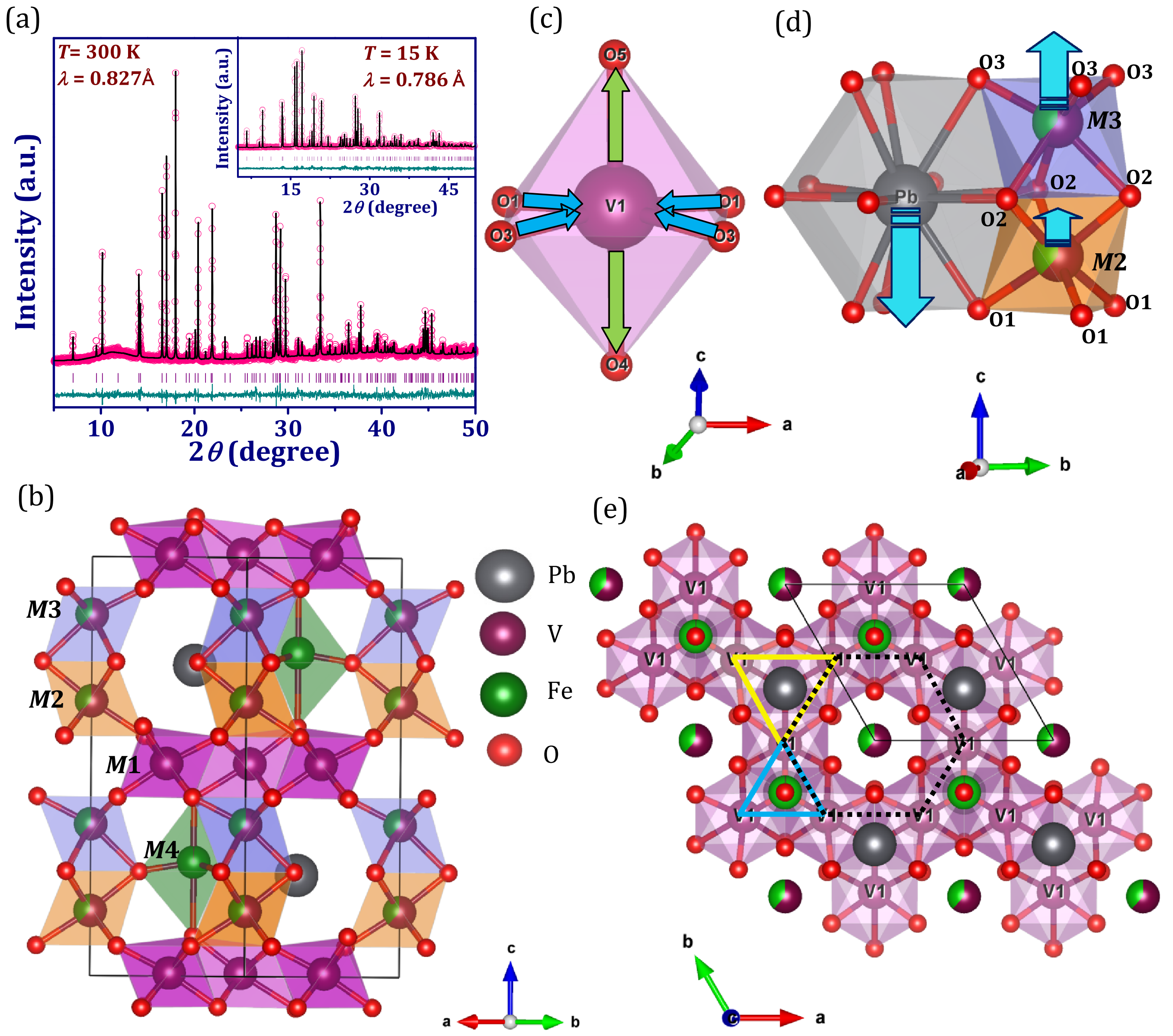

FIG. 1. (a) Rietveld refined 300K XRD pattern of PFVO. Inset: 15 K XRD data with fitting. Pink open circles represent the experimental data and solid black line represents the calculated pattern. The dark cyan line represents the difference between the observed and calculated pattern, while purple vertical lines signify the positions of the Bragg peaks. (b) Refined crystal structure. (c) A single $V(1)O_6$ octahedral unit with elongated V(1)-O bonds along z axis. (d) $M(2)M(3)O_9$ Face-shared dimer units connected with PbO_{12} cuboctahedron. Movements of the cation centers in the respective polyhedra are further shown by cyan arrows. (e) Kagome network formed by edge shared V(1) octahedra in the $a-b$ plane; two distinct corner-shared equilateral V(1) triangular motifs, designated by yellow triangle with longer V(1)-V(1) distances and sky blue triangle with shorter V(1)-V(1) distances.

resistivity set up (ARS CCR with current source (Keithley 6221) and nano-voltmeter (Keithley 2182). The $I-V$ characteristics were measured in dc mode with current source (Keithley 6221) and multimeter (Kiethley 2000).

III. RESULTS AND DISCUSSIONS

A. Bulk crystal structure and composition verification

Synchrotron x-ray diffraction data [Fig. 1(a)], collected from polycrystalline powder at both room temperature and 15 K, ensures pure single phase of the sample without any structural phase transition down to the lowest measured temperature, and consequently, satisfactory structural refinement has been performed by considering a noncentrosymmetric hexagonal $P6_3mc$ space group, which is consistent with the previous literature [32,33]. The refined structural parameters including lattice constants, atomic positions, site occupancy, along with the goodness factors are listed in Table I. The refined crystal structure is shown in Fig. 1(b), which shows that there are four distinct crystallographic sites [$M(1)$, $M(2)$, $M(3)$, and $M(4)$] for the transition metal (TM) cations, among which $M(1)$ forms Kagome network in the $a-b$ plane by edge-sharing $M(1)O_6$ octahedra. Our structural analysis clearly indicates that Fe completely substitutes

TABLE I. The sample is refined within a single crystallographic phase using a hexagonal space group $P6_3$mc. Lattice parameters at 300 K: $a = b = 5.746(4)$ Å, $c = 13.488(6)$ Å, $\alpha = \beta = 90^\circ$, $\gamma = 120^\circ$. $R_{wp} = 13.87$, $R_{\exp} = 9.27$, $\chi^2 = 2.24$. Lattice parameters at 15 K: $a = b = 5.719(7)$ Å, $c = 13.499(3)$ Å, $\alpha = \beta = 90^\circ$, $\gamma = 120^\circ$. $R_{wp} = 12.32$, $R_{\exp} = 8.44$, $\chi^2 = 2.13$.

		300 K					15 K				
Atoms	Wyckoff position	x	y	z	Occupancy	B (Å^2)	x	y	z	Occupancy	B (Å^2)
Pb	2b	0.333	0.667	0.242(3)	1.0	0.238(3)	0.333	0.667	0.240(3)	1.0	0.203(7)
V(1)	6c	0.510(2)	−0.510(2)	0.008(9)	1.0	0.241(7)	0.513(3)	−0.513(3)	0.008(7)	1.0	0.219(4)
V(2)	2a	0.000	0.000	0.155(7)	0.62	0.241(7)	0.000	0.000	0.156(3)	0.62	0.219(4)
Fe(2)	2a	0.000	0.000	0.155(7)	0.38	0.241(7)	0.000	0.000	0.156(3)	0.38	0.219(4)
V(3)	2a	0.000	0.000	0.362(6)	0.62	0.241(7)	0.000	0.000	0.360(2)	0.62	0.219(4)
Fe(3)	2a	0.000	0.000	0.362(6)	0.38	0.241(7)	0.000	0.000	0.360(2)	0.38	0.219(4)
Fe(4)	2b	0.667	0.333	0.272(8)	1.0	0.241(7)	0.667	0.333	0.275(5)	1.0	0.219(4)
O(1)	6c	0.173(6)	−0.173(6)	0.072(3)	1.0	0.119(6)	0.173(5)	−0.173(7)	0.072(5)	1.0	0.105(6)
O(2)	6c	0.156(9)	−0.156(9)	0.750(1)	1.0	0.119(6)	0.156(7)	−0.156(5)	0.750(2)	1.0	0.105(6)
O(3)	6c	0.172(3)	−0.172(3)	0.427(5)	1.0	0.119(6)	0.172(1)	−0.172(2)	0.427(3)	1.0	0.105(6)
O(4)	2b	0.667	0.333	0.424(8)	1.0	0.119(6)	0.667	0.333	0.424(9)	1.0	0.105(6)
O(5)	2b	0.667	0.333	0.095(9)	1.0	0.119(6)	0.667	0.333	0.095(7)	1.0	0.105(6)

V at the trigonal bipyramidal $M(4)$ site, both $M(2)$ and $M(3)$ sites of the $M(2)M(3)O_9$ dimer are randomly occupied by the V/Fe, while the $M(1)$ site is solely occupied by V (see Table I), which agrees quite well with the Fe-site preference as observed in case of $SrV_{6-x}Fe_xO_{11}$ [34]. Further, we have checked the stoichiometry of this compound using SEM-EDX and it has been confirmed that our PFVO sample retains the cation stoichiometry at the target composition, i.e., Pb:Fe:V being very close to 1:1.75:4.25 within the given accuracy of the measurement. On the other hand, by performing iodometric titration we have identified the oxygen stoichiometry in our PFVO compound to be around $O_{11+\delta}$ ($\delta = 0.04$), clearly refuting presence of any noticeable oxygen off stoichiometry in our sample within the given accuracy of the measurement. The results obtained from both the SEM-EDX and iodometric titration therefore steadily affirm that the PFVO is devoid of significant crystal vacancies, defects and cation-off-stoichiometries.

Next it is observed that due to stereochemically active Pb^{2+} $6s^2$ lone pair, large structural distortions in terms of tilting, rotation and elongated/compressed TM-oxygen bond distances of the TM-oxygen polyhedra [see Figs. S1(a)–S1(d) within the Supplemental Material [35]), as well as large structural asymmetry via significant off-centering of the metal cations (see Figs. 1(c)–1(d), and Table II) are present in the structure. As displayed in Fig. 1(c) and Table II, it is evident that the $V(1)O_6$ octahedra possess Z_{out} type Jahn-Teller distortion through local Z-axis elongation of the apical V(1)-O bond lengths. On top of it, the 300 K refined crystal structure illustrates that the V(1) atom also gets significantly off-centered [see Fig. 1(c) and Table II] through the creation of dissimilar (i.e., long and short) V(1)-O distances in each of the three V(1)-O pairs of the $V(1)O_6$ octahedra. Most interestingly, such off-centering of V(1) cation completely disappears in the basal plane at 15 K, while the Z_{out} J-T distortion persists (Table II). On the other hand, the $M(2)$-O and $M(3)$-O distances clearly indicate that both the $M(2)$ and $M(3)$ octahedra remain J-T inactive, but, significant shifting of the $M(2)$ and $M(3)$ cation centers is envisioned in the direction opposite to that of Pb center [see Fig. 1(d) and Table II]. Furthermore, the V(1) ions of the edge-shared $V(1)O_6$ octahedra, forming regular kagome lattice in the $a - b$ plane, get displaced from their respective octahedral centers as a result of large octahedral distortions and structural asymmetry at the $P6_3mc$ space group, thereby, forming kagome trimers consisting of two distinct sets of corner-shared V(1) equilateral triangular networks, one having longer V(1)-V(1) and the other with shorter V(1)-V(1) distances [Fig. 1(e)].

B. Local structural study

It is well known that the chemical order at the local scale may differ from the long-range order probed by crystallography [31,36–38], therefore the Fe and V K-edge EXAFS measurements have been carried out on this sample in order to probe the local atomic structure and chemical order around the respective cations.

1. Fe K-edge EXAFS analysis

As a matter of fact, the degree of local chemical order may become largely different from the long-range

TABLE II. V(1)-/$M(2)$-/$M(3)$-/Fe(4)-O bond distances at 300 K and 15 K.

Metal-O	Bond length (Å) 300 K	Shift 300 K	Bond length (Å) 15 K	Shift (Å) 15 K
V(1)-O(4)	2.09	0.14	2.10	0.17
V(1)-O(5)	1.95		1.93	
2 × V(1)-O(1)	1.88	0.04	1.90	0.00
2 × V(1)-O(3)	1.92		1.90	
3 × $M(2)$-O(2)	2.01	0.05	2.00	0.06
3 × $M(2)$-O(1)	2.06		2.06	
3 × $M(3)$-O(3)	1.92	0.25	1.93	0.22
3 × $M(3)$-O(2)	2.17		2.15	
3 × Fe(4)-O(2)	1.78		1.77	
Fe(4)-O(4)	2.05	0.33	2.05	0.34
Fe(4)-O(5)	2.38		2.39	

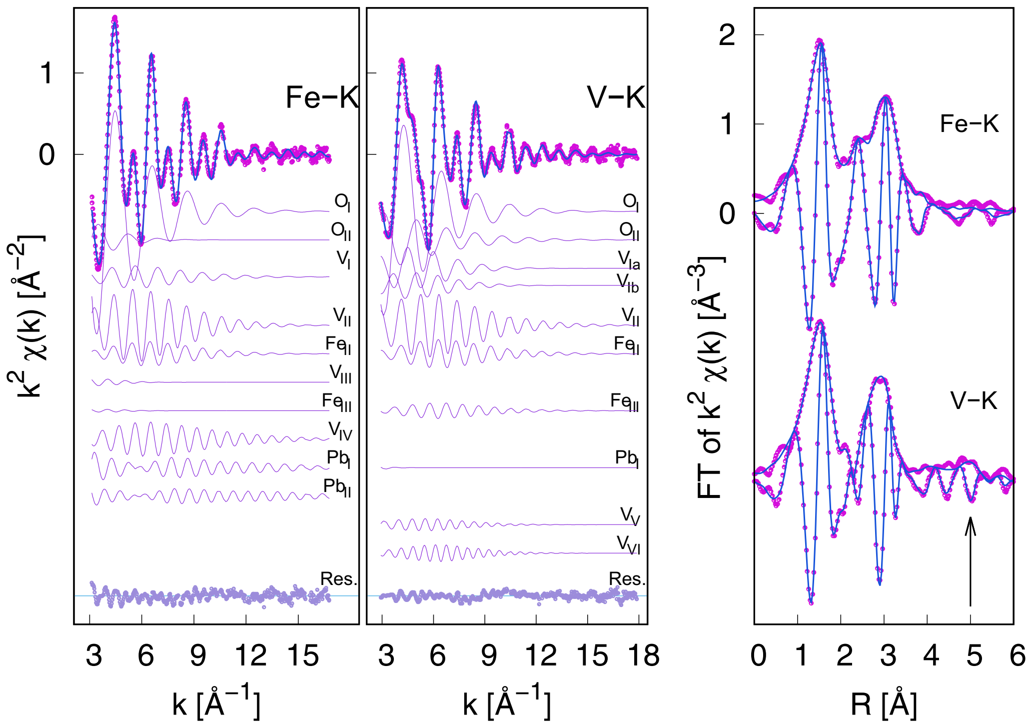

FIG. 2. Fe and V K-edge EXAFS fitting results. Left: Experimental data (violet dots) best-fit (blue line) are shown in k space. Individual single scattering paths (light violet lines) used in the analysis and the residual k^2 χ_{exp}- k^2 χ_{teo} are also presented, vertically shifted for clarity. Right: k^2-weighted Fourier transform (FT) moduli $|FT|$ and imaginary part of experimental data (violet dots) along with the respective best fit curves (blue lines).

crystallographic one. Eventually the antisite defects or different degree of chemical disorder at the local atomic scale commonly occur in various magnetic oxides, which are often elusive to x-ray diffraction techniques [31,36–39]. Chance of such site-exchange is even higher in the present system, as both Fe and V have very similar ionic sizes in their octahedral sites. EXAFS is one perfectly suitable chemically selective and local atomic structure sensitive technique to probe local atomic distributions. The collected Fe K-edge x-ray absorption spectra were processed with the ESTRA program [29] using the standard procedure for the background subtraction, data normalization and extraction of the EXAFS signal: the pre-edge background was modelled with a straight line calculated by fitting the experimental data in the interval 7000–7088 eV before the edge. The edge energy (E_0) was chosen at the first inflection point of the absorption edge, to define the photoelectron wave number $k = \hbar^{-1}\sqrt{2m_e(E-E_0)}$ (m_e being the electron mass). The post-edge atomic absorption background (μ_0) was calculated by performing an N-knots polynomial spline fitting through the data. The structural EXAFS signal was finally calculated as: $\chi_{\text{exp}}(k) = (\mu(k)\text{-}\ \mu_0(k))/(\mu_0(k))$. The quantitative analysis of the EXAFS signal was performed with the FitEXA program [29] by fitting the k^3-weighetd EXAFS spectrum (in the 3–16 Å^{-1} range) to the model curve calculated using the standard EXAFS formula [40] as a sum of Gaussian shaped coordination shells. The phases, amplitude, and mean free path functions were calculated using FEFF 8.2 program [40].

The $PbFe_{1.75}V_{4.25}O_{11}$ structure obtained from Rietveld refinement is complex with four different crystallographic sites partially occupied by Fe/V (Table I). Therefore the experimental EXAFS signal is expected to result from the superimposition of the structural signals of Fe in each crystallographic site, plus each signal being weighted by the Fe-site occupancy. In addition, the Fe_i-$(V/Fe)_j$ next-neighbor shell contributions from jth shells around the ith Fe site may be affected by local chemical order, which may be different from the average long-range chemical order as obtained from XRD analysis. Such a structural complexity makes the quantitative analysis of Fe K-edge EXAFS data of $PbFe_{1.75}V_{4.25}O_{11}$ sample a difficult task and opportune constraints to the refinement parameters in order to keep reduced number of free parameters becomes a necessity.

The Fourier transform modulus $|FT|$ (see right-side panel of Fig. 2) depicts two main peaks roughly representing the radial distribution function around the average Fe absorber, uncorrected for the phase shift that squeezes the observed distances by roughly 0.5 Å. The first $|FT|$ peak around 1.5 Å is attributed to the average Fe-O nearest-neighbor shell, the second $|FT|$ peak around 3 Å is mainly due to next-neighbor heavy scatterers, namely V, Fe, and Pb, while the structural signal from the Fe-O next-neighbor shells is expected to be negligibly weak due to weak oxygen scattering amplitude and its broad distribution. Multiple scattering contributions further did not appear relevant for the present analysis. It is really very important to note that the local structural disorder along with the photoelectron mean free path, the spherical wave attenuation term $1/R^2$ and the interference of several contributions, make the $|FT|$ signal almost negligible beyond 4 Å.

In order to achieve stable and reliable best fit we started from the crystallographic model, obtained from the Rietveld analysis, which have been used to distinguish the local environment around each Fe site (Table S1 within the Supplemental Material [35]). The neighboring atoms were grouped in coordination shells through a trial end error procedure selecting neighboring ions at similar distances. Consequently, for each shell the average-neighbor distances (R) and coordination numbers (N) were calculated, and finally the best fit agreement was statistically checked and the physical meaning of the structural parameters was also verified.

For each shell the crystallographic average distance was calculated as: $R = \sum_{i=1}^{4} R_i N_i M_i O_i / \sum_{i=1}^{4} N_i M_i O_i$, where the sums run over the four Fe crystallographic sites with R_i, N_i, M_i, and O_i being the distances, the numbers of neighbours, the crystallographic-site multiplicity and occupancy, respectively. From the crystallographic model, the Fe-O nearest neighbours can be grouped into two Fe-O shells at $R_{O_I} \approx$ 1.93 Å with multiplicity $M_{O_I} = 4.2$, and at $R_{O_{II}} = 2.32$ Å with multiplicity $M_{O_{II}} = 1.2$. The multiplicities were calculated as $M_O = \sum_{i=1}^{4} N_i M_i O_i / \sum_{i=1}^{4} M_i O_i$. These multiplicities M_{Oi} were kept fixed during the EXAFS data fit, while R_{Oi} and the mean square relative displacement (MSRD, σ^2) factors were refined.

The crystallographic model also individuates two main contributions for Fe-Pb next neighbours at around $R_{Pb_I} \simeq$ 3.35 Å (multiplicity $M_{Pb_I} = 1.7$) and at around $R_{Pb_{II}} \simeq 3.6$ Å (multiplicity $M_{Pb_{II}} = 1.3$). The multiplicities M_{Pb_i} were also kept fixed during the EXAFS data fit, while R_{Pb_i} and MSRD factors were refined.

For the Fe-V/Fe next-neighbor shells the model distances were calculated in the similar way but the multiplicity numbers had to be taken into account for the V/Fe chemical order in the neighboring sites: $M_x = \sum_{i=1}^{4} N_{ix} M_i O_i p_x / \sum_{i=1}^{4} M_i O_i$, where p_x is the probability of finding an atom x (x = V or Fe) in the neighbor site and therefore p_x is taken into account for getting an idea about the local chemical order. In case of random distribution of Fe and V at the respective sites p_x is the crystallographic occupancy of that site. On the contrary, if Fe-x correlation is favoured (disfavoured) p_x increases (decreases). The crystallographic model individuated four main Fe-V/Fe contributions at $R_{V/Fe_I} \simeq 2.79$ Å($M_{Fe_I} = 0.2$, $M_{V_I} = 0.3$), at $R_{V/Fe_{II}} \simeq 3.5$ Å($M_{Fe_{II}} = 1.3$, $M_{V_{II}} = 3.7$), at $R_{V/Fe_{III}} \simeq 3.66$ Å($M_{Fe_{III}} = 1.8$, $M_{V_{III}} = 2$), and at $R_{V/Fe_{IV}} \simeq 3.9$ Å($M_{Fe_{IV}} = 0.2$, $M_{V_{IV}} = 2.0$). In each shell the R and MSRD parameters for the Fe-V$_i$ and Fe-Fei contributions were constrained to equal. The attempt to fit the EXAFS spectrum by fixing the multiplicity numbers to the crystallographic values resulted a good best-fit agreement (see Fig. 2), and the shell distances closely match with the crystallographic model (Table III). In the next-neighbor the V/Fe$_{III}$ shell, expected around 3.7 Å, is found to be very weak due to a high MSRD, likely arises due to the effect of disorder and/or superimposition to other contributions neglected in the approximations assumed. The Fe-Pb shell distances result slightly expanded with respect to the crystallographic model.

TABLE III. Structural results obtained from the Fe K-edge EXAFS fitting. Fixed or constrained parameters are indicated by (∗), the uncertainty on the last digit of refined parameters are reported in parenthesis. The multiplicity numbers (N_{Cryst}) and average distances (R_{Cryst}) expected from the crystallographic model are reported for sake of comparison.

Shell	N	N$_{\mathrm{crystal}}$	R (Å)	R$_{\mathrm{crystal}}$ (Å)	σ^2 (10^{-2})(Å^2)
Fe-O$_I$	4.2∗	4.2	1.928(5)	1.92	0.99(5)
Fe-O$_{II}$	1.2∗	1.2	2.32(2)	2.28	1.09(5)
Fe-V$_I$	0.6(1)	0.3	2.83(2)	2.79	0.88(7)
Fe-Fe$_I$		0.2		2.79	
Fe-V$_{II}$	3.7∗	3.7	3.46(2)	3.51	0.90(5)
Fe-Fe$_{II}$	1.3∗	1.3	3.46∗	3.51	0.90∗
Fe-V$_{III}$	2.0∗	2.0	3.69∗	3.66	6.5(3)
Fe-Fe$_{III}$	1.3∗	1.3	3.69∗	3.66	6.5∗
Fe-V$_{IV}$	2.0∗	2.0	3.93(2)	3.91	0.69(5)
Fe-Fe$_{IV}$		0.2		3.95	
Fe-Pb$_I$	1.7∗	1.7	3.43(3)	3.35	0.66(5)
Fe-Pb$_{II}$	1.3∗	1.3	3.76(4)	3.61	0.54(5)

In order to check the chemical order the multiplicity numbers for Fe-Fe and Fe-V contributions in each shell were left free to vary with respect to their crystallographic values in the opposite way: $M'_{Fe_i} = M_{Fe_i} + x$ and $M'_{V_i} = M_{V_i}$ - x. We should comment on the fact that while random Fe/V model is confirmed in case of Fe-Fe/V$_{II-IV}$ shells, the best fit reduced χ^2_v factor and the AIC (akaike information criterion) number [29,41] decrease by more than 10% by refining the multiplicity number of the Fe- V/Fe_I nearest shell at around 2.8 Å, pointing out some preferential V occupancy of the nearest metal site around Fe (N(Fe-V1) = 0.6, N(Fe-FeI) = 0, Table S1 within the Supplemental Material [35]) and may suggest some Fe at the $M1$ site. A simulation on top of it shows that 0.05 Fe occupancy at the $M1$ site and preferred Fe-V chemical order is consistent with the EXAFS finding. Noticeably XRD analysis is insensitive to such weak Fe occupancy at $M1$ site.

In summary, the EXAFS analysis confirms the average local structure around Fe ions, which is consistent with the crystallographic structure. EXAFS analysis also suggests some minor disorder due to 0.05 Fe-occupancy at the $M1$ site.

2. V K-edge EXAFS analysis

For the analysis of the V K-edge EXAFS spectra we adopted the same procedure described above along the scheme reported in Table S1 within the Supplemental Material [35]. The best fit is presented in Fig. 2 and the refined parameters are reported in Table IV. About 70% of V resides on the $M1$ sites forming wide-edge sharing VO$_6$ octahedra sheets. Noticeably the Fourier transform depict an evident contribution in the 5 Å region (uncorrected for the phase shift) corresponding to V-V next-neighbor correlations in the V$_I$O$_6$ sheets (V-V$_V$ and V-V$_{VI}$ shells in Table IV), which are evidently absent in the Fe-EXAFS spectra. Interestingly, the first V-O$_{I,II}$ coordination shells depart from the crystallographic model. Firstly, in order to fit the V EXAFS data we had to refine their coordination numbers, we constrained the total V-O coordination number to the crystallographic value: $N_{O_I} + N_{O_{II}} = 6$ obtaining $N_{O_I}/N_{O_{II}}$ ratio around 2. Moreover we need to refine a different energy shift for the O$_{II}$ shell resulting –2.5(1) eV below the energy shift of the O$_I$ shell. This finding suggests

TABLE IV. Structural results obtained from the V K-edge EXAFS fitting. The estimated uncertainty on the last digit of refined parameters are reported in parenthesis. The multiplicity numbers (N_{crystal}) and average distances (R_{Cryst}) expected from the crystallographic model are reported for sake of comparison. (∗) fixed or constrained parameters, (∗∗) the coordination numbers of the V-O nearest shells were left free to vary, constrained to the total V-O coordination number: $N_{OI} + N_{OII} = 6$. Edge energy shift was $\Delta E = -0.7(1)$ eV for all the contributions, except O_{II} having $\Delta E_{OII} = -3.2(1)$ eV.

Shell	N	N_{crystal}	R (Å)	R_{crystal} (Å)	σ^2 (10^{-2})(Å^2)
V-O_I	4.3(3)	5.5	1.961(5)	1.96	0.92(5)
V-O_{II}	1.7∗∗	0.5	2.30(3)	2.19	0.72(5)
V-V_I	1.5∗	1.5	2.64(2)	2.71	1.6(1)
V-V_I	1.4∗	1.4	3.04(2)	3.05	1.6(1)
V-V_{II}	3.3∗	3.3	3.49(2)	3.50	0.73(5)
V-Fe_{II}	1.5∗	1.6	3.49∗	3.50	0.73∗
V-Fe_{III}	1.2∗	1.2	3.75(2)	3.65	0.85(5)
V-Pb_{II}	1.5∗	1.5	3.59(5)	3.66	3.2(2)
V-V_V	2.6∗	2.6	4.98(2)	5.00	1.4(1)
V-V_{VI}	5.0∗	5.0	5.55(3)	5.42	1.2(1)

the longer V-O_{II} shell is associated to lower valence V^{3+} sites, likely at the $M2$ and $M3$ sites, while shorter V-O_I shell is associated to the higher valence V^{4+} of $M1$ sites.

C. Estimation of transition metal's valence state

1. Bond valence sum calculation (BVS)

From the structural analysis we get four different "V/Fe" sites. Therefore, to authenticate these site-specific valence states of V, we have carried out bond valence sum calculation (BVS) using the formula $VS = \sum \exp((R_0\text{-}R_i)/\mathrm{b})$, where VS is the valence state of the cation, R_i is the observed bond length, R_0 is the ideal bond length when the element i has exact valence 1 and b is an empirical constant, typically 0.37 Å, the results of which are tabulated in Table V. In case of PFVO, the $M(1)$, $M(2)$, and $M(3)$ sites retain the V-oxidation states at +4, +3, and +3, respectively, which is in contrast to AV_6O_{11} (A = Na, K, Sr, Pb) compounds [23,42] (see Table V).

2. Valence state determination from XANES (x-ray absorption near edge structure)

It is known that both Fe and V often get stabilized in more than a single oxidation state [21,43–45], and therefore to confirm the charge states, the Fe K- as well as V K-edge XANES have been collected and presented in Figs. 3(a) and 3(d). The measured Fe K-XANES spectra [see Fig. 3(a)] is quite identical in shape and structure to the Fe_2O_3 one [46], suggesting 3+ oxidation state of Fe in our sample. Further, to know the true oxidation state and coordination of Fe, the pre-edge peak has been fitted after subtracting background (fixing at arctangent shape), as shown in Fig. 3(b). The energy position of the pre-edge peak centroid and the pre-edge peak integrated intensity obtained from fitting, have been plotted in Fig. 3(c) (see solid yellow circle), along with those of the standards adopted from the studies by Giuli *et al.* [47] and Wilke *et al.* [48]. These values strongly suggest the average Fe coordination to be in between 5-fold and 6-fold within its 3+ oxidation state. This finding is consistent with the distorted Fe-O nearest-neighbor distribution found from XRD and EXAFS analysis consisting of a bimodal distribution of Fe-O bonds resulting from a combination of distorted octahedra and 5-fold coordinated sites and thereby, maintaining an average coordination number of 5.4 (see Table III).

In order to maintain the charge neutrality of the PFVO sample, V should carry an average of 3.47+ valence, i.e., a mixture of 3+ and 4+ oxidation states maintaining a specific ratio of V^{3+}:V^{4+} $\sim$ 2.25:2. So to ensure the V-charge state in this sample, the V K-edge XANES spectrum has been collected and shown in Fig. 3(d). Qualitatively this spectrum resembles quite well with that of V_4O_7 [49], a mixed V^{3+}/V^{4+} oxide with an average "V" valence to be around +3.5. Further, in order to get quantitative understanding of V valence in this sample the experimental V-K-edge XANES spectra are compared between PFVO and the reference V-oxides, as shown in Fig. 3(d). The edge energy shift as a function of V valence is evident, where the PFVO edge energy appears in between the V^{3+} and V^{4+} spectra. In order to evaluate the V valence state in PFVO sample the experimental XANES spectra have been fitted using a sigmoid shaped step function(s), to reproduce the raising of the edge step, plus gaussian (g) peaks to reproduce the pre-edge features. The nominal edge energies E_0^i were selected at the inflection point of the sigmoid functions. For V-oxides we found the E_0^i linearly increasing by 2.3(1) eV per valence charge unit resulting in the average V charge to be 3.6(1) eV in PFVO.

D. Magnetization and heat capacity

Now we focus on the magnetic properties of PFVO. The temperature (T) variations of the dc magnetic susceptibility χ have been measured in the zero-field-cooled (ZFC), field-cool-cooling (FCC), and field-cool-heating (FCH) protocols

TABLE V. Wycokff positions and corresponding valence states of V for AV_6O_{11} (A = Na, K, Sr, Pb) [23,42] compounds, and also valence states of V/Fe for the PFVO obtained from bond valence sum calculations in this paper.

Site	Wycokff positions	Na/KV_6O_{11}	SrV_6O_{11}	PbV_6O_{11}	$PbFe_{1.75}V_{4.25}O_{11}$ (BVS calculation)
$M(1)$	6c	V^{3+}	V^{3+}	V^{3+}	V^{4+}
$M(2)$	2a	V^{4+}	V^{4+}	V^{4+}	V^{3+}/Fe^{3+}
$M(3)$	2a	V^{4+}	V^{4+}	V^{4+}	V^{3+}/Fe^{3+}
$M(4)$	2b	V^{4+}	V^{3+}	V^{3+}	Fe^{3+}

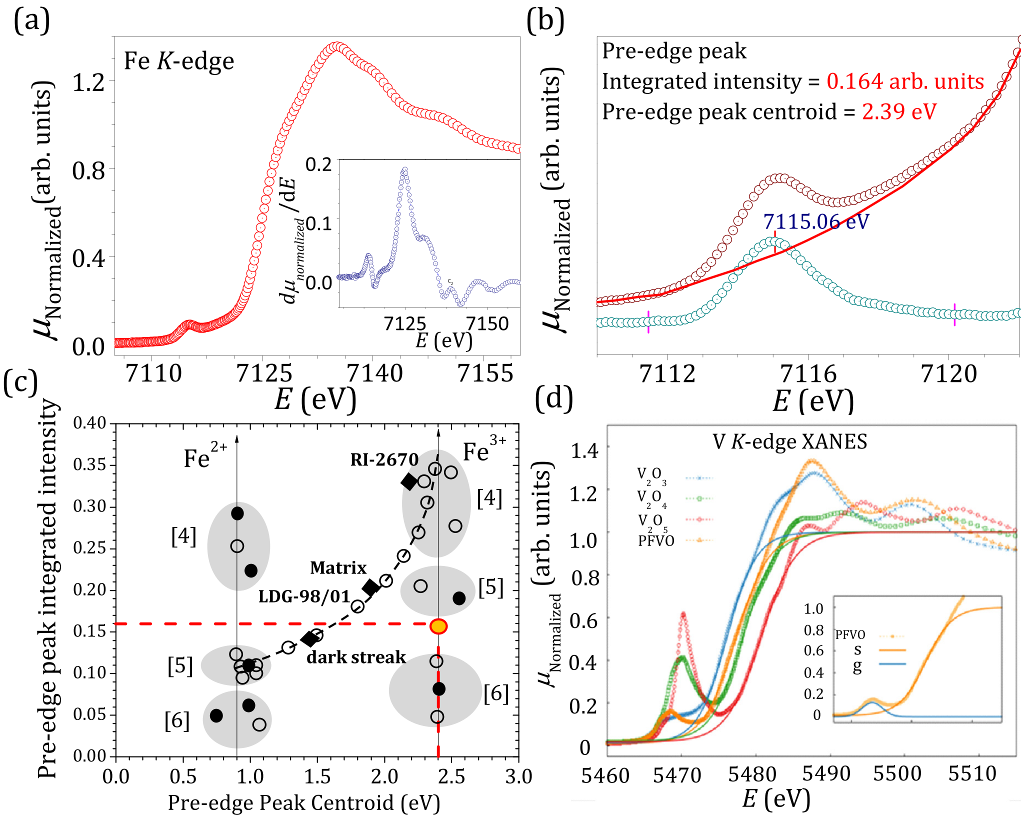

FIG. 3. (a) Fe *K*-edge XANES spectra (open red circles). Inset shows the first-derivative curve (open blue circles) of the normalized Fe *K*-absorption spectrum. (b) Illustration of the pre-edge peak (open dark cyan circles), after subtracting the background (solid red line) from the normalized experimental absorption spectrum (open wine circles), indicating centroid energy position and the integrated intensity of the pre-edge peak. (c) Integrated intensity of the pre-edge peak is plotted against the centroid energy position for a variety of Fe-based reference samples, showing a range of Fe-valences and local coordination geometry around Fe. This figure is adopted from Phys. Rev. B **27**, 4 (1983); the solid yellow circle corresponds to the centroid energy position and integrated intensity for our PFVO sample. (d) V *K*-edge XANES spectra of PFVO and reference V-oxides. The experimental spectra (dots) have been fitted to a sigmoid shaped step function (s) (full lines) to reproduce the raising of the edge step, plus gaussian (g) peaks to reproduce the pre-edge features. An example of XANES fitting for PFVO spectrum is presented in the insert.

under three different applied magnetic fields (0.01 Tesla, 0.05 Tesla, and 0.2 Tesla), and the 0.01 Tesla $\chi(T)$ data are presented in Fig. 4(a). A steep upturn is evident near around 85 K in both the observed ZFC and FC data [see $d\chi/dT$ vs T, shown in the inset to Fig. 4(a)]. In order to comment on the nature of this transition the temperature-dependent heat capacity (C_p vs T) has been measured [see Fig. 4(b)], where the absence of any anomaly in the C_p data strongly refutes long-range coherent magnetic order [50–53]. However, the temperature-dependent inverse susceptibility variation ($1/\chi$ versus T) under 0.01 Tesla field shows a sharp downturn below about 275 K, and a gradual smearing out of the same with increasing applied fields [see inset to Fig. 4(b)], signifying the presence of short-range ferromagnetic correlations within the paramagnetic background. Isothermal remanent magnetization (IRM) at 15 K and the temperature-dependent ac susceptibility at a set of discrete frequencies ranging from 21 Hz to 1111 Hz have been carried out using conventional method. It is evident that the M_{IRM} undergoes a slow decay [Fig. 4(c)], and the obtained M_{IRM} vs t data is further fitted using the logarithmic function, $M_{IRM}(t)/M(0) = A_0 - S * \ln(1 + t/t_0)$, as illustrated in Fig. 4(c), which is a signature of magnetic materials having hysteretic magnetization and/or glassy dynamics [53–55]. Further, the temperature variations of both the in-phase and out-of-phase susceptibilities $\chi'(\omega, T)$ and $\chi''(\omega, T)$ [see Fig. 4(d)] show a well-defined maximum at ∼85 K, which has a clear frequency dispersion, thereby affirming the spin-glass ground state [56–58]. Considering the two distinct corner-shared equilateral V(1) triangular units within the kagome network [see Fig. 4(e)], competing FM [via V(1)-V(1) direct exchange pathway of the shorter triangle] and AFM [(via V(1)-O-V(1) superexchange pathway of the longer triangle] spin arrangements as well as disordered distributions of V and Fe within $M(2)$ and $M(3)$ sites, the spin-glass ground state of this compound below 85 K can be explained. In addition it is worthwhile to note that due to randomly occupied Fe^{3+} and V^{3+} ions at the $M(2)$ and $M(3)$ sites, the Fe^{3+} (d^5:$t_{2g}^3e_g^2$) sitting at the $M(2)/M(3)$ sites prefer antiferromagnetic super exchange interactions with its neighboring V^{4+} of the common corner shared $V(1)O_6$ octahedra (Fe^{3+}-O-V^{4+}) according to Goodenough-Kanamori rule [59].

Apart from the short-range FM correlation and the spin-glass magnetic ground state, distinct thermal hysteresis

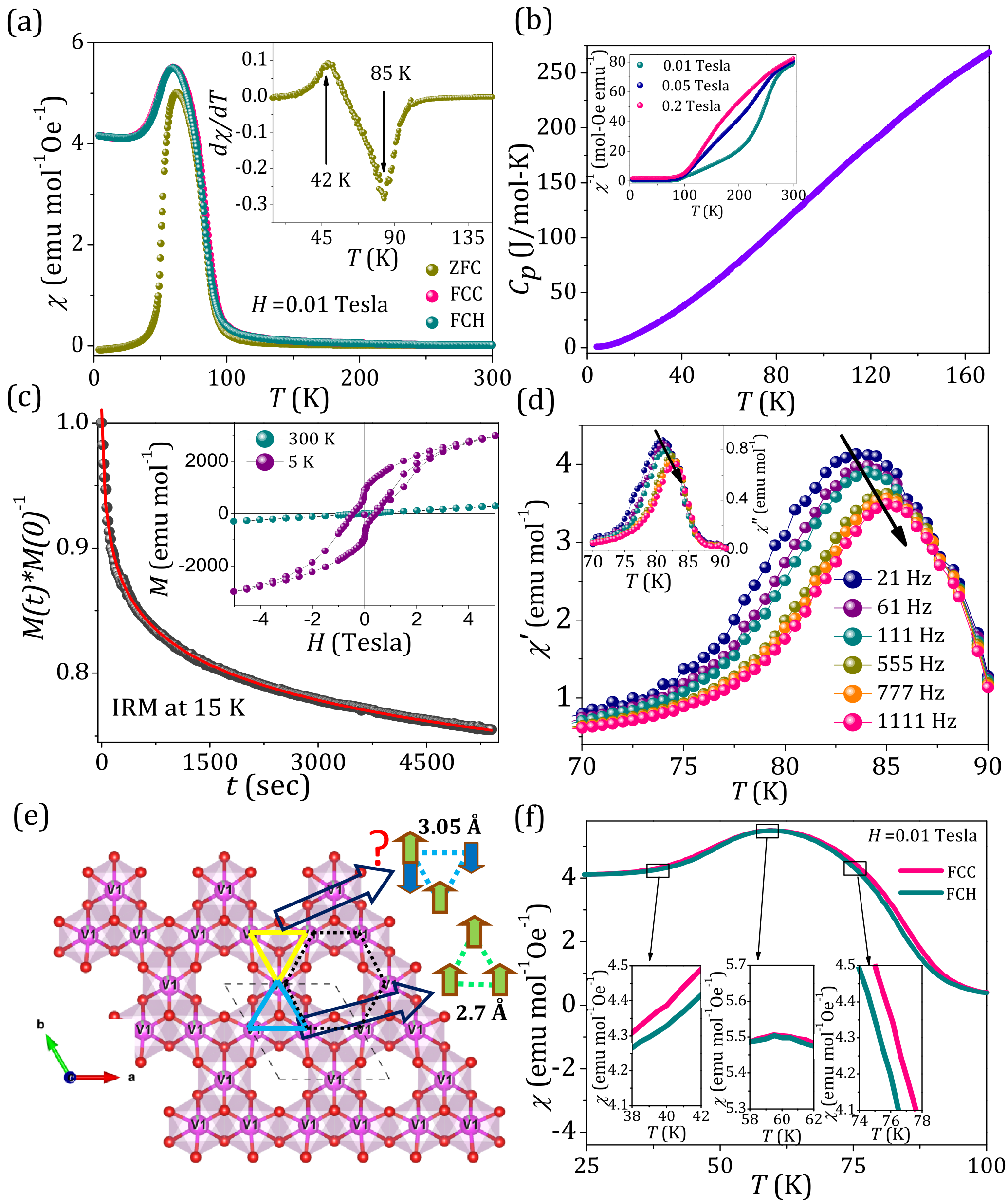

FIG. 4. (a) Zero-field-cooled (ZFC), field-cool-cooling (FCC) and field-cool-heating (FCH) dc magnetic susceptibility variations as a function of temperature [$\chi(T)$] under) 0.01 Tesla applied magnetic field. Inset: Respective first-order temperature derivative of the FCH susceptibility variation. (b) Temperature-dependent zero-field heat capacity C_p vs T data. Inset: Temperature-dependent inverse magnetic susceptibility variations for three different magnetic fields. (c) The relaxation nature of isothermal remanent magnetization (shaded black circles) as a function of time at $T = 15$ K along with the respective fitting (red solid line). Inset: 5 K (shaded magenta circles) and 300 K (shaded dark cyan balls) $M - H$ curves. (d) The temperature dependence of the in-phase ac susceptibility component $\chi'(T)$ at the different applied frequencies. Inset: The respective out-of-phase susceptibility $\chi''(T)$ variations. (e) The edge-shared V(1) octahedral units forming a Kagome network in the *ab* plane; the solid sky blue (yellow) colored lines represent the corner shared V(1) equilateral triangular motifs having short (long) V(1)-V(1) bond distances. (f) Zoom-in view of the temperature-dependent 0.01 Tesla FCC and FCH susceptibility variations, indicating thermal hysteresis between the heating and cooling data.

between the FCC and FCH magnetization is observed [see Fig. 4(f)]. Interestingly, the FCC and FCH data do show clear thermal hysteresis at least at two temperature regions [∼95–62 K and ∼45–30 K, as highlighted in Fig. 4(f)]. Further, the thermal hysteresis around T_C is relatively widely extended in the temperature span, and the FCC and FCH lines cross each other at two temperatures ≈ 60 K and 48 K. Such divided hysteresis loop could be an indication of multiple first-order phase transitions [60].

E. Electrical resistivity

Next we investigate the temperature-dependent electrical resistivity ($\rho - T$) of this sample at various electric currents,

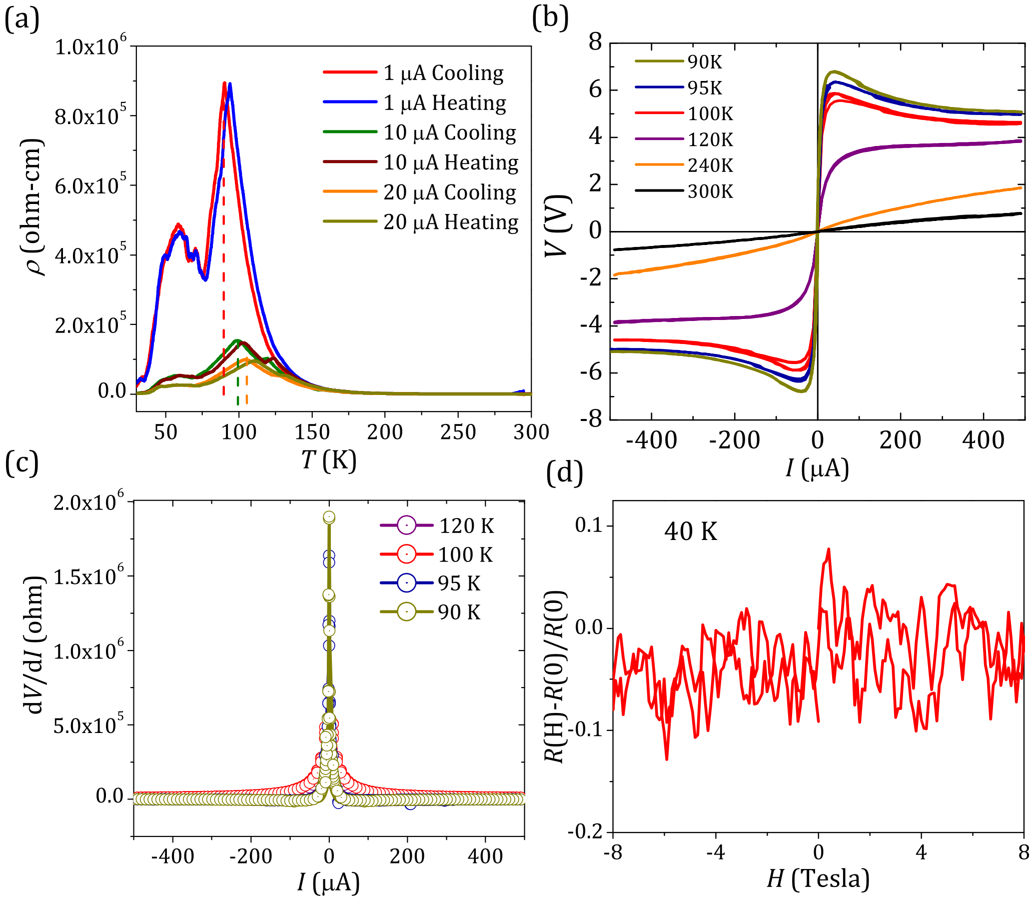

FIG. 5. (a) Temperature-dependent electrical resistivity at three different electric currents. (b) Voltage vs current ($I - V$) characteristic at various temperatures in dc current mode. (c) First-order derivative of the measured $I - V$ curves at some selected temperatures, (d) Magnetic field-dependent magnetoresistance (MR) at 40 K.

and the measured $\rho - T$ data for three different currents have been presented in Fig. 5(a) for both the cooling and heating cycles. The higher temperature insulating nature ($d\rho/dT < 0$) of transport is followed by a sharp metal-insulator transition (MIT) in the form of a strong suppression of resistivity at the onset of magnetic transition for the lowest current (1 μA). In PFVO, the mixed V^{3+}/V^{4+} valency and the completely random distribution of V and Fe in the $M(2)$ and $M(3)$ sites of the crystal structure introduce various magnetic exchange interaction pathways through face-, edge-, and corner-shared polyhedral connectivity in between the $M(i)$ ($i = 1$ to 4) sites. This facilitates the microscopically intrinsic electronic phase separation within the system. Like perovskite manganites, such electronic inhomogeneity in PFVO could be associated with the competition between the correlated-metal and the Mott-insulating phases [61].

With decreasing temperature from 300 K, a continuous increase in the resistivity till the appearance of the sharp downturn in the $\rho - T$ curve signifies insulating transport in that specific temperature range. Due to tilting distortions of the V(1)O$_6$ octahedra and the consequent local Z-axis elongation [see in Fig. 6(b)], a collective Z_{out} Jahn-Teller (J-T) distortion gets stabilized at the V(1) center at higher temperature. This J-T effect eventually lifts degeneracy of the t_{2g} orbitals of the V^{4+} (t_{2g}^1) cation in the V(1) site [Fig. 6(b)], thereby resulting in the half-filled low-lying doubly degenerate d_{xz}, d_{yz} orbitals and higher energy empty d_{xy} level. As a result of which the t_{2g}^1 electron occupies any of the two degenerate levels (d_{zx}/d_{yz}) maintaining an orbital disorder situation. But interestingly, on top of the J-T distortion, the V(1) cation shows a significant off-centering movement in the xy basal plane, creating further splitting in the doubly degenerate d_{zx}/d_{yz} orbitals and giving rise to the orbital ordering of the t_{2g}^1 electron. So, the t_{2g}^1 electron occupies the lower energy $d_{zx}(d_{yz})$ orbital keeping the higher energy $d_{yz}(d_{zx})$ level empty providing an energy gap in between them, and hence an orbital ordered insulating (OOI) state is emerged at the high temperatures. Besides, the observed insulating resistivity within the given temperature region could be interpreted in terms of the enhanced carrier scattering by localized spin fluctuations in the OO state and resultant spatial randomness of the transfer interaction [$t_{ij} \sim \cos(\Delta\theta_{ij}/2)$], with t_{ij} being transfer integral between the neighboring atomic sites and $\Delta\theta_{ij}$ is the relative angle of the local spins), i.e., off-diagonal disorder effect [62]. Following insulating resistivity the sample undergoes insulator to metal transition through orbital disordering and shows a strong suppression in the resistivity magnitude upon temperature lowering. It should be noted that there is competition between the J-T distortion plus off-centering assisted orbital ordering/disordering of V^{4+} ion [Figs. 6(b), 6(c), and 1(c) along with Table II] in the V(1) kagome layer and the spatially random ferromagnetic exchange pathway

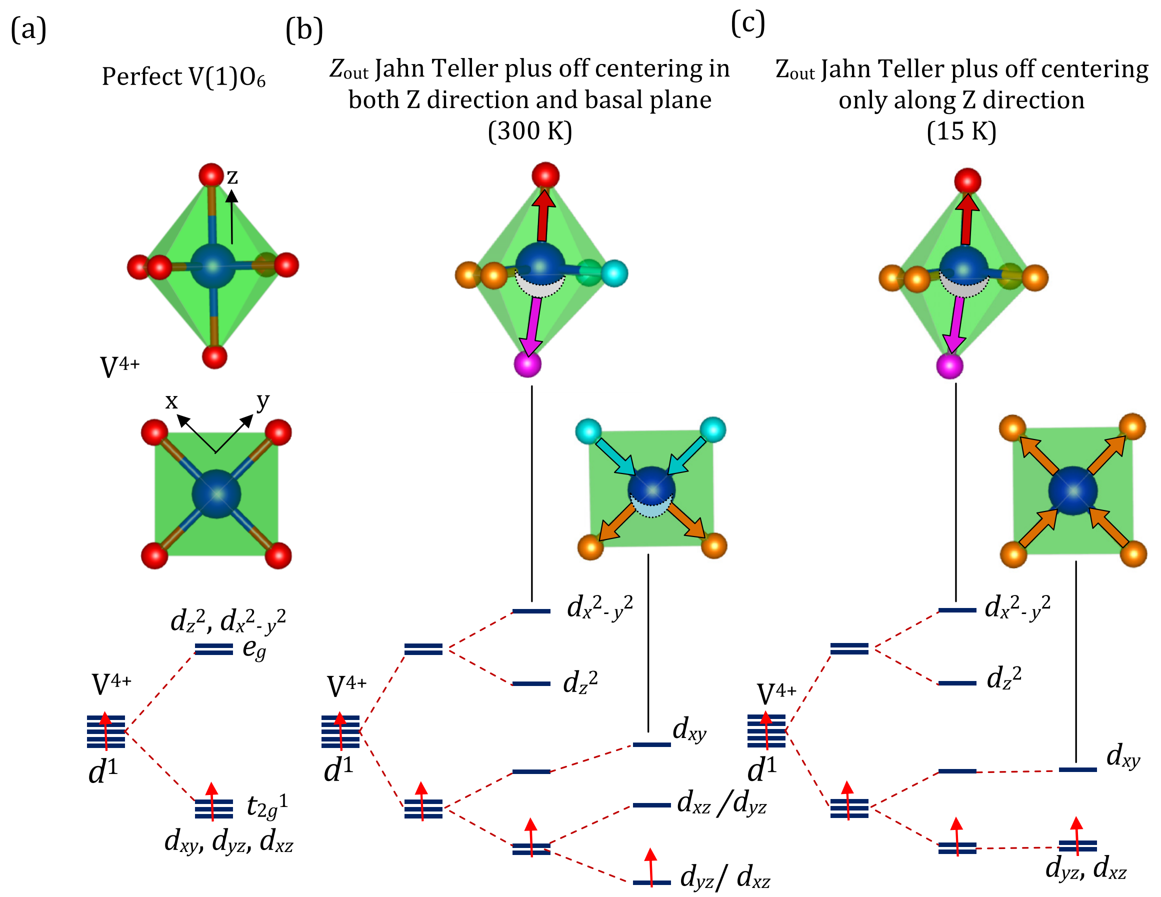

FIG. 6. (a) Perfect V(1)O$_6$ octahedra and corresponding energy level diagram. (b) Z_{out} Jhan-teller distortion along Z axis and off centering movement of V(1) along Z axis and within basal plane at 300 K, and the derived energy levels. (c) Z_{out} Jahn-Teller distortion along Z axis and off centering movement of V(1) only along Z axis at 15 K with the corresponding energy level diagram.

driven weakening of spin-disorder scattering within V(1)O$_6$ and V(2)V(3)O$_9$ layers. Therefore, one may point towards the fact that at the onset of ferromagnetic transition (T_c) the developed short-range ferromagnetic correlation suppresses the spin-disorder-scattering effect, thereby facilitating electron conduction in the material. In addition, this electron conduction is further accelerated with temperature lowering due to the disappearance of V(1)-off-centering movement in the basal plane [see Fig. 6(c) and Table II] and the subsequent suppression of energy-level splitting between the d_{zx} and d_{yz} orbitals. The t_{2g}^1 electron therefore prefers to be arranged in degenerate d_{zx}/d_{yz} orbitals at low temperatures, favoring orbital disordering and consequent metallic band structure [11–13,16,63–65].

F. Current-induced change in electrical resistivity

Now we turn our focus on the temperature-dependent electrical resistivity measurements under different applied electrical currents (1 μA, 10 μA, and 20 μA). The measured $\rho - T$ data are illustrated in Fig. 5(a). In addition to the MIT, a few intriguing aspects regarding the observed current-induced spectacular changes in electrical resistivity are summarized as follows:

(1) The occurrence of hysteresis between the heating and cooling cycles of the $\rho - T$ curves in all the currents.

(2) Appearance of a few weak extra features by further lowering the temperature from MIT is evident.

(3) The gradual decrease in the maximum value of resistivity at the onset of MIT, and simultaneously a systematic shift in the MIT temperature towards higher values with increasing electric current [shown in Fig. 5(a)].

It is already discussed that at the low-current region, the relative competition between the orbital ordering/disordering and the ferromagnetic interaction driven suppression of spin-disorder scattering is responsible for the observed MIT. So, even at a small applied dc current (1 μA) there is melting of OO state in the vicinity of T_c, giving rise to the insulator-metal transition through a huge reduction in the measured resistance [66–68]. Now with increasing current the electric field above a critical value further helps to destabilize the orbital ordering in this sample from even higher temperatures. Such an unusual behavior is the outcome of a delicate balance between J-T effect, ferromagnetic exchange, electric field, thermal energy, and orbital ordering/disordering. The observed systematic decrease in the measured maximum resistivity at the onset of MIT by orders of magnitude as well as the gradual shift of the metal-insulator transition towards higher temperatures with increasing current can be designated as the colossal electroresistance (CER) phenomenon. In order to check the accuracy of this quite extraordinary CER phenomenon, we have verified our results on several different samples and also by changing the order of the applied current during the measurement (see Fig. S2 within the Supplemental Material [35]). We have also measured current-voltage $(I - V)$ characteristics at different temperatures and the results for some selected temperatures along with the respective derivative curves (dv/dI vs I) are depicted in Figs. 5(b) and 5(c), which further confirm the CER. The collected $I - V$ curves possess ohmic nature of conduction at higher temperatures while transforming into non-ohmic character at lower temperatures. In addition, the dV/dI vs I [Fig. 5(c)] curves clearly indicate that with increasing current there is reduction in the electrical resistance, thereby supporting the CER behavior in PFVO. Further, as displayed in Fig. 5(b), voltage shows a sharp increase at lower currents followed by a maximum before decreasing at higher currents, thus signifying the well known negative differential resistance (NDR) behavior [66]. It is important at this point to confirm the intrinsic origin of the observed CER behavior against the possibility of the extrinsic effect of Joule heating. We therefore also checked the true origin of CER in this sample (detailed discussion on testifying the role of joule heating is presented in the Supplemental Material [35].). We find that the sample temperature vary only within 0.5 K of the respective set temperatures during the current/voltage sweeps (see Fig. S3 within the Supplemental Material [35]), signifying the effect of Joule heating to be insignificant, and hence establishing purely intrinsic origin of the observed electrical responses. Generally, the CER-related observations on the application of electric current (field) could emerge collectively from (1) the decrease in spin-disorder scattering, (2) the growth of the domains giving rise to better metallic path, as explained by double exchange mechanism where metallic conduction is coupled with FM interactions, (3) increasing mean-free path of electrons, and (4) growth of aligned domains in applied field giving rise to decrement in the probability for domain-wall scattering [69]. Therefore, it is likely that the applied external electric field stimulates melting of V(1) orbital ordering by suppressing the V(1) off-centering movement [see Fig. 6(c)], thereby causing delocalization of intrasite holes through the generation of mobile electronic charges, and ensuring the MIT and CER phenomena in PFVO.

Finally, the observed hysteresis between the heating and cooling cycles of the resistivity curves [Figs. 5(a)] likely originates due to the coexistence of two competing phases, namely, orbital ordered Mott insulator and orbital disordered correlated FM metal, thereby identifying the MIT as first-order in nature [70–72]. Furthermore, a few weak extra features appear at lower temperatures in the $\rho - T$ curve [Fig. 5(a)], supporting the existence of multiple first-order phase transitions, which is in agreement with the observations from temperature-dependent dc susceptibility measurements [Fig. 5(f)].

But surprisingly unlike perovskite manganites, no magnetoresistance is observed (up to 8 Tesla) in the electrical resistivity in this sample, negating the existence of double exchange driven colossal magnetoresistance to be coexisting with CER [see Fig. 5(d)]. Clearly, the emergence of CER phenomenon in PFVO has no electronic connection with the CMR in the present case [73,74]. Instead of having a magnetically long-range ordered ground state like manganites, the presently studied PFVO sample possesses the spin-glass magnetic ground state due to the competing FM and AFM interactions as well as disordered distributions of V and Fe within the $M(2)$ and $M(3)$ sites of the crystal structure. The spin-glass magnetic ground state induces random freezing of spins due to the dominance of anisotropy energy over the specially random short-range ferromagnetic interactions. However, no double exchange mediated CMR and the related CER, as happens in certain manganites, could be applicable to explain the CER of PFVO.

IV. CONCLUSION

In this paper the structural, electronic, magnetic, and transport properties of polycrystalline $PbFe_{1.75}V_{4.25}O_{11}$ sample are experimentally studied in detail. We verified the sample quality by performing SEM-EDX and iodometric titration measurements, which clearly reveal almost perfectly maintained cation compositions as well as the near absence of any noticeable oxygen-offstoichionetry, defects, stacking faults, etc., in our PFVO polycrystalline material. The relative proportion of the mixed vanadium valency (V^{3+} with respect to V^{4+} upon ~30% Fe-doping), revealed from the V K-edge XANES measurement, strongly modifies the carrier concentration and places this particular composition of the AV_6O_{11} series as an electronic analog to the hole-doped manganites. Our detailed electrical transport measurements clearly affirm the metal-insulator transition (MIT) and colossal electroresistance (CER) phenomena in the system. Further, the intrinsic nature of the observed MIT and CER phenomena has been authenticated by changing the order of the applied current during electrical resistivity measurements, negating the presence of Joule heating, as well as performing the $\rho - T$ measurements on different batches of PFVO powder samples. The ferromagnetic interactions driven weakening of spin-disorder scattering and the externally applied electric field together help the delocalization of the charge carriers, which eventually act against the structural distortion driven stabilization of orbital ordering, thereby promoting a subtle competition between the orbital ordered and disordered states, which is at the root of all the observed spectacular electrical properties in this compound. On the other hand, our in-depth dc and ac magnetization measurements confirm the spin-glass magnetic ground state in PFVO.

ACKNOWLEDGMENTS

R.A.S. and A.B. thank CSIR, India, and IACS for fellowships. A.B. also acknowledges SERB, DST for the National Postdoctoral Fellowship (File No. PDF/2020/000785). S.R. thanks DST for funding (Grant No. CRG/2019/003522). The authors also thank Indo-Italian POC for support to carry out experiments in Elettra, Italy, and Laboratory for Materials and Structures, Tokyo, Japan for providing experimental facilities through collaborative research project. S.R also thanks the Technical Research Center (TRC) of IACS for experimental facilities.

[1] M. Imada, A. Fujimori, and Y. Tokura, Rev. Mod. Phys. **70**, 1039 (1998).
[2] Y. Tokura and N. Nagaosa, Science **288**, 462 (2000).
[3] H. C. Nguyen and J. B. Goodenough, Phys. Rev. B **52**, 324 (1995).
[4] K. Gupta, P. Mahadevan, P. Mavropoulos, and M. Ležaić, Phys. Rev. Lett. **111**, 077601 (2013).
[5] J. Kanamori, J. Phys. Chem. Solids **10**, 87 (1959); J. Appl. Phys. **31**, S14 (1960).
[6] K. I. Kugel and D. I. Khomskii, Sov. Phys. Usp. **25**, 231 (1982).
[7] G. Khaliullin, Prog. Theor. Phys. Suppl. **160**, 155 (2005).
[8] C. Ulrich, G. Khaliullin, J. Sirker, M. Reehuis, M. Ohl, S. Miyasaka, Y. Tokura, and B. Keimer, Phys. Rev. Lett. **91**, 257202 (2003).
[9] G. R. Blake, T. T. M. Palstra, Y. Ren, A. A. Nugroho, and A. A. Menovsky, Phys. Rev. Lett. **87**, 245501 (2001); Phys. Rev. B **65**, 174112 (2002).
[10] Y. Ren, T. T. M. Palstra, D. I. Khomskii, E. Pellegrin, A. A. Nugroho, A. A. Menovsky, and G. A. Sawatzky, Nature (London) **396**, 441 (1998).
[11] M. Reehuis, C. Ulrich, P. M. Abdala, P. Pattison, G. Khaliullin, J. Fujioka, S. Miyasaka, Y. Tokura, and B. Keimer, Phys. Rev. B **94**, 104436 (2016).
[12] J. Fujioka, S. Miyasaka, and Y. Tokura, Phys. Rev. B **72**, 024460 (2005).
[13] S. Miyasaka, T. Okuda, and Y. Tokura, Phys. Rev. Lett. **85**, 5388 (2000).
[14] Y. Shimizu, K. Okai, M. Itoh, M. Isobe, J.-I. Yamaura, T. Yamauchi, and Y. Ueda, Phys. Rev. B **83**, 155111 (2011).
[15] S. Kim, B. H. Kim, K. Kim, and B. I. Min, Phys. Rev. B **93**, 045106 (2016).
[16] S. Miyasaka, Y. Okimoto, M. Iwama, and Y. Tokura, Phys. Rev. B **68**, 100406(R) (2003).
[17] Y. Motome, H. Seo, Z. Fang, and N. Nagaosa, Phys. Rev. Lett. **90**, 146602 (2003).
[18] Z. Fang and N. Nagaosa, Phys. Rev. Lett. **93**, 176404 (2004).
[19] A. M. Oleś, P. Horsch, and G. Khaliullin, Phys. Rev. B **75**, 184434 (2007).
[20] M. E. de Roy, J. P. Besse, R. Chevalier, and M. Gasperin, J. Solid State Chem. **67**, 185 (1987).
[21] Y. Kanke, F. Izumi, E. Takayama-Muromachi, K. Kato, J. Kamiyama, and H. Asano, J. Solid State Chem. **92**, 261 (1991).
[22] O. Mentre and F. Abraham, J. Solid State Chem. **125**, 91 (1996).
[23] Y. Kanke, Phys. Rev. B **60**, 3764 (1999).
[24] T. Naka, T. Matsumoto, Y. Kanke, and K. Murata, Physica B: Condens. Matter **206**, 853 (1995).
[25] Y. Hata, Y. Kanke, E. Kita, H. Suzuki, and G. Kido, J. Appl. Phys. **85**, 4768 (1999).
[26] A. Maignan, O. I. Lebedev, G. Van Tendeloo, C. Martin, and S. Hébert, Appl. Phys. Lett. **96**, 232502 (2010).
[27] J. Rodriguez Carvajal, Physica B: Condens. Matter **192**, 55 (1993).
[28] A. Di Cicco, G. Aquilanti, M. Minicucci, E. Principi, N. Novello, A. Cognigni, and L. Olivi, J. Phys. Conf. Ser. **190**, 012043 (2009).
[29] C. Meneghini, F. Bardelli, and S. Mobilio, Nucl. Instrum. Methods Phys. Res. Sect. B **285**, 153 (2012).
[30] S. Middey, P. Aich, C. Meneghini, K. Mukherjee, E. V. Sampathkumaran, V. Siruguri, P. Mahadevan, and S. Ray, Phys. Rev. B **94**, 184424 (2016).
[31] A. Bandyopadhyay, S. K. Neogi, A. Paul, C. Meneghini, I. Dasgupta, S. Bandyopadhyay, and S. Ray, Phys. Rev. B **95**, 024432 (2017).
[32] A.-C. Dhaussy, O. Mentré, F. Abraham, and Y. Calage, J. Solid State Chem. **147**, 609 (1999).
[33] O. Mentré, A.-C. Dhaussy, F. Abraham, and H. Steinfink, J. Solid State Chem. **130**, 223 (1997).
[34] Y. Hata, Y. Kanke, K. Ohoyama, and E. Kita, J. Phys. Soc. Jpn. **78**, 054703 (2009).
[35] See Supplemental Material at http://link.aps.org/supplemental/10.1103/PhysRevB.104.045149 for connectivites of different polyhedra, table for EXAFS fitting method, thermal variation of resistivity at 100 μA and 1 μA, detailed discussion on testifying the role of joule heating, and schematic representation of the sample space during the electrical transport measurement.
[36] P. Aich, C. Meneghini, and S. Ray, Mater. Res. Express **6**, 026103 (2019).
[37] C. Meneghini, S. Ray, F. Liscio, F. Bardelli, S. Mobilio, and D. D. Sarma, Phys. Rev. Lett. **103**, 046403 (2009).
[38] A. Nag, S. Jana, S. Middey, and S. Ray, Indian J. Phys. **91**, 883 (2017).
[39] M. Das, P. Dutta, S. Giri, S. Majumdar, A. Bandyopadhyay, A. K. Yadav, S. N. Jha, D. Bhattacharyya, G. Das, and V. Rajaji, Phys. Rev. B **101**, 064419 (2020).
[40] J. J. Rehr and R. C. Albers, Rev. Mod. Phys. **72**, 621 (2000).
[41] C. Meneghini, F. Bardelli, S. Mobilio, and C. Prestipino, Estra and Fitexa, *International Tables for Crystallography, Volume I, X-ray Absorption Spectroscopy and Related Techniques* (to be published).
[42] O. Mentré, Y. Kanke, A.-C. Dhaussy, P. Conflant, Y. Hata, and E. Kita, Phys. Rev. B **64**, 174404 (2001).
[43] D. Wilson and M. A. Langell, Appl. Surf. Sci. **303**, 6 (2014).
[44] L. Xie, S. Liu, C. Gao, R. Cao, J. Cao, C. Sun, and Z. Su, Inorg. Chem. **46**, 7782 (2007).
[45] C. A. Bridges and J. E. Greedan, J. Solid State Chem. **177**, 1098 (2004).
[46] L. A. Grunes, Phys. Rev. B **27**, 2111 (1983).
[47] G. Giuli, E. Paris, G. Pratesi, C. Koeberl, and C. Cipriani, Meteorit. Planet. Sci. **38**, 1181 (2003).
[48] M. Wilke, F. Farges, P.-E. Petit, J R. G. E. Brown, and A. Martin, Am. Mineral. **86**, 714 (2001).
[49] J. Wong, F. W. Lytle, R. P. Messmer, and D. H. Maylotte, Phys. Rev. B **30**, 5596 (1984).
[50] C. R. Wiebe, J. E. Greedan, P. P. Kyriakou, G. M. Luke, J. S. Gardner, A. Fukaya, I. M. Gat-Malureanu, P. L. Russo, A. T. Savici, and Y. J. Uemura, Phys. Rev. B **68**, 134410 (2003).
[51] S. Rayaprol, K. Sengupta, and E. V. Sampathkumaran, Phys. Rev. B **67**, 180404(R) (2003).
[52] N. Mohapatra, K. K. Iyer, S. Rayaprol, and E. V. Sampathkumaran, Phys. Rev. B **75**, 214422 (2007).
[53] S. Middey, S. Ray, K. Mukherjee, P. L. Paulose, E. V. Sampathkumaran, C. Meneghini, S. D. Kaushik, V. Siruguri, K. Kovnir, and D. D. Sarma, Phys. Rev. B **83**, 144419 (2011).
[54] S. Majumdar, E. V. Sampathkumaran, D. Eckert, A. Handstein, K.-H. Müller, S. R. Saha, H. Sugawara, and H. Sato, J. Phys.: Condens. Matter **11**, L329 (1999).
[55] D. X. Li, S. Nimori, Y. Shiokawa, Y. Haga, E. Yamamoto, and Y. Onuki, Solid State Commun. **120**, 227 (2001).

[56] J. Mydosh, *Spin Glasses: An Experimental Introduction* (Taylor and Francis, London, 1983).

[57] C. Dekker, A. F. M. Arts, H. W. de Wijn, A. J. van Duyneveldt, and J. A. Mydosh, Phys. Rev. B **40**, 11243 (1989).

[58] C. Dekker, A. F. M. Arts, H. W. de Wijn, A. J. van Duyneveldt, and J. A. Mydosh, Phys. Rev. Lett. **61**, 1780 (1988).

[59] P. W. Anderson, Phys. Rev. **79**, 350 (1950).

[60] A. Banerjee, J. Sannigrahi, S. Giri, and S. Majumdar, Phys. Rev. B **98**, 104414 (2018).

[61] E. Dagotto (ed.), *Nanoscale Phase Separation and Colossal Magnetoresistance* (Springer, Berlin, 2002); E. Dagotto, T. Hotta, and A. Moreo, Phys. Rep. **344**, 1 (2001); A. Moreo, S. Yunoki, and E. Dagotto, Science **283**, 2034 (1999).

[62] A. Urushibara, Y. Moritomo, T. Arima, A. Asamitsu, G. Kido, and Y. Tokura, Phys. Rev. B **51**, 14103 (1995).

[63] P. Horsch and A. M. Oleś, Phys. Rev. B **84**, 064429 (2011).

[64] M. Kasuya, Y. Tokura, T. Arima, H. Eisaki, and S. Uchida, Phys. Rev. B **47**, 6197 (1993).

[65] S. Yamamoto, D. Ootsuki, D. Shimonaka, D. Shibata, K. Kodera, M. Okawa, T. Saitoh, M. Horio, A. Fujimori, H. Kumigashira, K. Ono *et al.*, J. Phys. Soc. Jpn. **87**, 024708 (2018).

[66] A. Guha, N. Khare, A. K. Raychaudhuri, and C. N. R. Rao, Phys. Rev. B **62**, R11941 (2000); A. Guha, A. Ghosh, A. K. Raychaudhuri, S. Parashar, A. R. Raju, and C. N. R. Rao, Appl. Phys. Lett. **75**, 3381 (1999).

[67] Y. Tokura (ed.), *Colossal Magnetoresistive Oxides* (Gordon & Breach Science Publishers, Singapore, 2000); C. N. R. Rao, and B. Raveau (eds.), *Colossal Magnetoresistance, Charge Ordering and Related Properties of Manganese Oxides* (World Scientific, Singapore, 1998).

[68] Y. Tokura, Rep. Prog. Phys. **69**, 797 (2006).

[69] T. Wu, S. B. Ogale, J. E. Garrison, B. Nagaraj, A. Biswas, Z. Chen, R. L. Greene, R. Ramesh, T. Venkatesan, and A. J. Millis, Phys. Rev. Lett. **86**, 5998 (2001).

[70] A. Asamitsu, Y. Tomioka, H. Kuwahara, and Y. Tokura, Nature. Lett. **388**, 50 (1997).

[71] A. Bhaskar, M.-S. Huang, and C.-J. Liu, RSC Adv. **7**, 11543 (2017).

[72] A. Camjayi, C. Acha, R. Weht, M. G. Rodríguez, B. Corraze, E. Janod, L. Cario, and M. J. Rozenberg, Phys. Rev. Lett. **113**, 086404 (2014).

[73] A. K. Debnath and J. G. Lin, Phys. Rev. B **67**, 064412 (2003).

[74] H. Jain, A. K. Raychaudhuri, Ya. M. Mukovskii, and D. Shulyatev, Appl. Phys. Lett. **89**, 152116 (2006).